Microstructure and heteroatom dictate doping mechanism and thermoelectric properties of poly(alkyl-chalcogenophenes)

Madeleine P. Gordon,[1,2#] Shawn A. Gregory,[3#] Jamie P. Wooding,[3] Shuyang Ye,[4] Gregory M. Su,[5,6] Dwight Seferos,[4] Mark D. Losego,[3] Jeffrey J. Urban,[1*] Shannon Yee,[7*] and Akanksha K. Menon[7*]

1. The Molecular Foundry, Lawrence Berkeley National Laboratory, Berkeley, CA, 94720, USA.
2. Applied Science and Technology Graduate Group, University of California, Berkeley, CA, 94720, USA.
3. School of Materials Science and Engineering, Georgia Institute of Technology. Atlanta, Georgia 30332, USA
4. Department of Chemistry, University of Toronto, 80 St. George Street, Toronto, Ontario M5S 1A1, Canada
5. Materials Sciences Division, Lawrence Berkeley National Laboratory, Berkeley, CA 94720, USA.
6. Advanced Light Source, Lawrence Berkeley National Laboratory, Berkeley, CA 94720, USA.
7. G.W. Woodruff School of Mechanical Engineering, Georgia Institute of Technology. Atlanta, Georgia 30332, USA

# These authors contributed equally.
* Corresponding authors: jjurban@lbl.gov; shannon.yee@me.gatech.edu; akanksha.menon@me.gatech.edu

Abstract: Heteroatom substitution is one promising way to favorably alter electronic transport in conductive polymers to improve their performance in thermoelectric devices. This study reports the spectroscopic, structural, and thermoelectric properties of poly(3-(3',7'-dimethyloctyl) chalcogenophenes) (P3RX) doped with 2,3,5,6-tetrafluoro-7,7,8,8-tetracyanoquinodimethane (F4TCNQ), where the doping methodology, the heteroatom (X = Thiophene (T), Selenophene (Se), Tellurophene (Te)) and the extent of doping are systematically varied. Spectroscopic measurements reveal that while all P3RX polymers are appreciably doped, the doping mechanism is inherently different between the polymers. Poly(3-hexylthiophene) (P3HT, used in this study as a control) and P3RTe doped primarily via integer charge transfer (ICT), whereas P3RSe and P3RT appear to be doped via charge-transfer complex (CTC) mechanisms. Despite these differences, all polymers saturate with roughly the same number of F4TCNQ counterions (1 dopant per 4 to 6 heterocycles), reinforcing the idea that the extent of charge transfer from polymer to dopant varies significantly on the preferred doping mechanism. Grazing incidence wide-angle X-ray scattering measurements provide insight into the structural driving forces behind these different doping mechanisms - P3RT and P3RSe have similar microstructures in which F4TCNQ intercalates between the π-stacked backbones resulting in CTC doping (localized charge carriers), while P3HT and P3RTe have microstructures in which F4TCNQ intercalates in the alkyl-side chain region, giving rise to ICT doping (delocalized charge carriers). These structural and spectroscopic observations shed light on why P3HT and P3RTe obtain maximum electrical conductivities *ca*. 3 S/cm, while P3RT and P3RSe obtain maximum electrical conductivities <10^{-3} S/cm under the same thin film processing conditions. Ultimately, this work quantifies the effects of heteroatom, microstructural ordering, extent of doping, and doping mechanism on optical and electronic properties and provides rational guidance for designing future polymer and dopant chemistries for high performance thermoelectric materials.

Semiconducting polymers are an attractive class of materials for optical and electronic devices where processability and mechanical flexibility are desired.[1-3] Integration of these polymers into thermoelectric devices, used for energy harvesting and/or localized heating and cooling, has risen in popularity over the last decade.[2,4,5] P3HT (poly(3-hexylthiophene)) is a promising, well-studied p-type organic semiconducting polymer, but its electrical conductivity (σ) and Seebeck coefficient (S) fall short of conventional inorganic materials, thereby limiting P3HT's practical use in thermoelectric devices. One avenue for improving electronic performance is through polymer main chain heteroatom substitution; the heteroatom identity can fine-tune the molecular packing and the frontier molecular orbital energies, both of which influence charge transport properties.[6-9] In a previous study, we demonstrated that substituting the heteroatom in poly(alkyl-chalcogenophenes) from S to Se to Te results in smaller optical band gaps and increases the susceptibility to $FeCl_3$ oxidation, *i.e.,* a smaller amount of dopant is needed.[10,11] This in turn yields an optimal thermoelectric power factor ($S^2\sigma$) of *ca.* 13 μW/mK^2 for poly(alkyl-tellurophenes) that achieve appreciable σ and low S values (*ca.* 50 S/cm and 30 μV/K, respectively) that are indicative of high doping levels. This previous work demonstrated that heteroatom substitution can alter doping susceptibility and thermoelectric performance, but fundamental insights into the doping-induced charge transfer mechanisms and resulting structure-property relationships for this class of poly(alkyl-chalcogenophenes) remain unexplored.

Chemical doping involves oxidizing or reducing the polymer main chain, thus altering the density and filling of electronic states. Additionally, dopant geometry,[12] dopant intercalation in the polymer microstructure,[13,14] and the alignment of polymer and dopant frontier molecular orbital energies[15,16] must also be considered when engineering a polymer/dopant system.[17] While $FeCl_3$ is commonly used for oxidative doping, its relatively small molecular size (~3-6 Å) can make it challenging to track the dopant position and interactions with the semiconducting polymer.[15] On the other hand, the molecular oxidant F4TCNQ (2,3,5,6-tetrafluoro-tetracyanoquinodimethane) is suitable for quantifying doping mechanisms and establishing structure-doping relationships as its larger molecular size causes a greater disruption to the polymer's microstructure. Additionally, F4TCNQ has been shown to be an effective dopant for enhancing thermoelectric performance in a variety of ways,[18] including charge transfer complexation (CTC),[13] integer charge transfer (ICT),[19-21] and/or double doping[22] depending on the polymer microstructure, energy levels, and processing conditions. CTC involves the formation of new local hybridized molecular orbitals with a partial, non-integer charge transfer from the polymer to the dopant.[13] In contrast, ICT involves the transfer of an integer of charge (*e.g.* 1*e* or 2*e* transfer)[13] and leads to more electrically conductive materials as the polaronic carriers are not localized in a hybridized orbital between the polymer and dopant.[19] By engineering F4TCNQ to dope P3HT primarily through the ICT pathway and intercalate among the hexyl side chains, solution doping studies have reported electrical conductivities of 1-10 S/cm,[23-25] vapor doped conductivity of 1-100 S/cm,[26] and high-temperature rubbing-induced conductivities of >100 S/cm.[18] Unlike P3HT, its branched side chain analog P3EHT (poly(3-(2'-

ethyl)hexylthiophene)), is doped by F4TCNQ through a CTC pathway with dopant molecules intercalating between the π-stacks, which leads to a low electrical conductivity of 10^{-3} S/cm.[13] Despite having the same conjugated backbone as P3HT, this P3EHT study demonstrated that microstructural ordering significantly influences the doping mechanism and resulting optical and electronic properties.

Herein, we investigate the effects of heteroatom substitution, doping method, and dopant concentration on the resulting thermoelectric and charge transport properties of a series of poly(3-(3',7'-dimethyloctyl) chalcogenophenes), where the chalcogen is either S, Se, or Te (P3RT, P3RSe, P3RTe, respectively). Through optical, infrared and photoelectron spectroscopies, we find that F4TCNQ dopes P3RT primarily via CTC, P3RSe via both CTC and ICT, and P3RTe primarily via ICT. Experiments with P3HT are also performed and confirm that the doping and processing procedures are comparable to prior literature reports. Grazing incidence wide-angle x-ray scattering (GIWAXS) sheds light on the underlying cause for these different doping mechanisms. P3RT and P3RSe have similar structural ordering where F4TCNQ intercalates between the π-stacks, leading to primarily localized, CTC based doping. In contrast, P3RTe and P3HT have similar microstructural ordering with F4TCNQ primarily intercalating into the lamellar side chain region, resulting in more delocalized, ICT based doping. Thermoelectric measurements reveal the performance impacts of the different doping mechanisms; CTC dominated P3RT and P3RSe have low carrier mobilities and electrical conductivities ($\sigma < 10^{-2}$S/cm), whereas ICT dominated P3RTe and P3HT have considerably higher carrier mobilities and electrical conductivities ($\sigma \approx 3$S/cm) upon doping with F4TCNQ via both solution and vapor doping methods.

Thin films (*ca.* 300 nm) of each polymer were spin coated from toluene solutions. These films were either solution-doped with varying F4TCNQ molarities in acetonitrile or vapor-doped by subliming F4TCNQ for 60-minutes. Detailed experimental procedures and polymer characterization can be found in **Note S1**, and in our prior study.[10]

UV-Visible-Near Infrared (UV-Vis-NIR) spectroscopy is used to provide cursory evidence for the extent of doping and the mechanism as a function of dopant concentration and heteroatom. **Figure 1** plots the UV-Vis-NIR spectra for polymer thin films on glass substrates in their pristine, solution doped (50 mM), and vapor doped forms. In each panel of **Figure 1**, black lines show the pristine spectra, and the pink and blue lines represent the vapor and 50 mM solution doped films, respectively. An in-depth analysis of the UV-Vis-NIR spectra shown in **Figure 1** is provided in the supporting information (**Note S2**).

Figure 1 provides qualitative insight into the extent of doping; as the intensity of the pristine polymer π-π^* peak between 500-700 nm decreases, the extent of doping increases. For both the solution and vapor doped scenarios, P3RT is least susceptible to F4TCNQ doping (**Figure 1a**) and P3RSe demonstrates a stronger degree of doping (*i.e.,* greater π-π^* bleaching, **Figure 1b**). P3RTe (**Figure 1c**) shows the highest degree of F4TCNQ doping, and the optical features at 410 nm, 760 nm and 875 nm are indicative of ICT being the predominant doping mechanism at play.[19,27-29] While P3RSe also demonstrates these ICT features, peaks at 364 nm and 685 nm suggest the presence of CTC doping as well (**Figure 1b**).[19,27-29] In contrast, P3RT demonstrates predominantly CTC doping peaks (**Figure 1a**). To facilitate direct comparisons with prior literature, measurements were also made on P3HT films (**Figure 1d**), which demonstrate strong ICT features at 410 nm, 760 nm and 875 nm and a fair degree of F4TCNQ doping susceptibility, like P3RTe. Note that in all three P3RX films and P3HT films, there is little variation in the optical spectra of solution doped and vapor doped films, which suggests that the extent of doping is comparable with both methods.

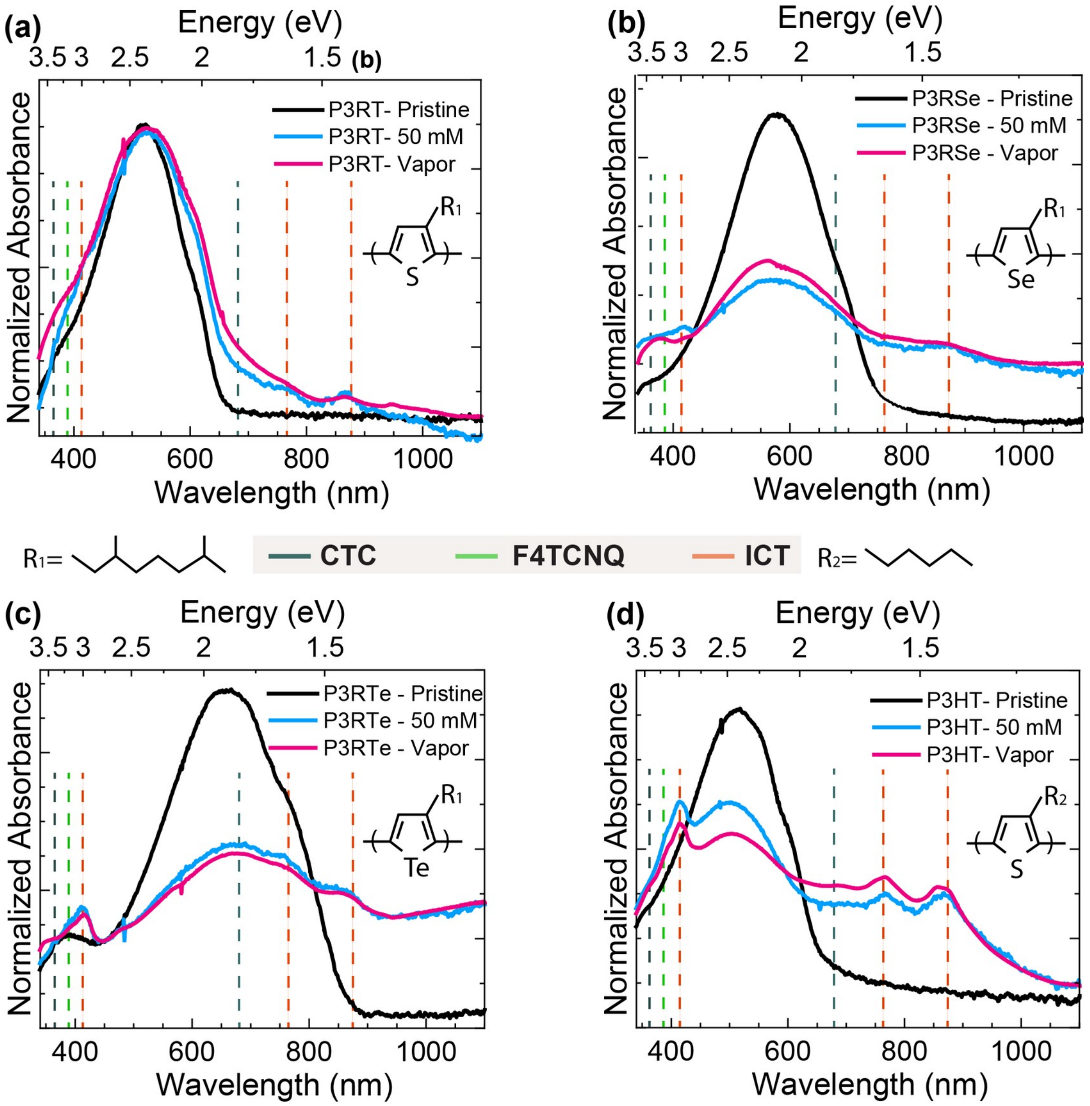

Figure 1: Normalized UV-Vis-NIR spectra of the pristine polymers, and the F4TCNQ solution doped (50 mM) and vapor doped films, (a) poly(3-(3’,7’-dimethyloctyl)thiophene) (P3RT), (b) poly(3-(3’,7’-dimethyloctyl)selenophene) (P3RSe), (c) poly(3-(3’,7’-dimethyloctyl)telurophene) (P3RTe), and (d) poly(3-hexylthiophene) (P3HT). The dashed lines in each panel show the peak locations of CTC (teal lines *ca.* 364, 685 nm), residual F4TCNQ dopant (green lines *ca.* 390 nm) and ICT (orange lines *ca.* 410, 760, 875 nm).

To corroborate these optical trends, attenuated total reflection Fourier-transform infrared spectroscopy (ATR-FTIR) was performed on these films. ATR-FTIR measurements can provide insights into the extent of doping (*via* polaronic absorbance in the mid-IR), degree of charge carrier delocalization (broad optical absorbance ranging from *ca*. 1500 cm^{-1} to over 5000 cm^{-1}) and the doping mechanism (*via* changes in the C ≡ N stretching mode absorbance near 2200 cm^{-1}). For the sake of brevity, full discussion on this technique is provided in **Note S3**. These measurements reveal that P3RTe and P3HT demonstrate strong peak intensities at 2194 cm^{-1} correlated with ICT, while P3RT has peak intensities between 2200-2015 cm^{-1} linked to CTC features, and P3RSe has intensities associated with both ICT and CTC absorption features. Overall, these ATR-FTIR results are consistent with the doping mechanisms elucidated by UV-Vis-NIR.

These optical and infrared spectroscopic measurements provide qualitative insight into the charge transfer mechanism but fail to quantify the extent of doping in the P3RX films and the relative contribution of each doping mechanism at play. To this end, X-ray photoelectron spectroscopy (XPS) surface profiling was used. **Figure 2a-d** shows the heteroatom spectra (S-2p, Se-3d, Te-3d) for the pristine polymer films, 50 mM solution doped films, and vapor doped films; additional XPS spectra are in **Note S4**. To provide insight into the dopant-polymer interactions, deconvoluted N-1s spectra for 50 mM doped films are shown in **Figure 2e**.

Upon doping there is a clear shift to higher binding energies, which is indicative of a loss in electron density with the introduction of dopant in **Figure 2a-d**. XPS heteroatom spectra confirm that vapor doping and 50 mM solution doping yield similar results based upon their analogous shifts in binding energy. In-depth discussion of heteroatom peak positions and their deconvolutions can be found in **Note S4**. In order to quantify the extent of doping, the atomic abundance for F and N with respect to the heteroatom (S, Se, Te) was used. We examine here the solution doped films due to the better stability of the dopant molecule under vacuum, leading to less background noise. We find that the dopant to heterocycle ratio for 50 mM doped P3RT is 19 ± 3 %, P3RSe is 19 ± 2 %, P3RTe is 23 ± 8 %, and P3HT is 18 ± 4 % (**Note S4**). These results suggest that each P3RX polymer has roughly equal amounts of F4TCNQ present at the film's surface (*ca.* 1 dopant per 5 rings), which is consistent with previous P3HT-F4TCNQ reports.[30,31] Inspection of the N-1s spectra shown in **Figure 2e** provides additional insight as Watts *et al.* studied ICT and CTC in P3HT doped with F4TCNQ and assigned the N^{-1} peak at 398.2 eV to ITC and the N^0 peak at 400 eV to CTC.[19] The motivation behind these assigned differences in binding energy arises from the electron density differences in F4TCNQ for these two doping mechanisms. ICT involves a full electron transfer to the F4TCNQ molecule, resulting in a higher electron density and thus a shift to lower binding energies, whereas CTC appears at higher binding energies.

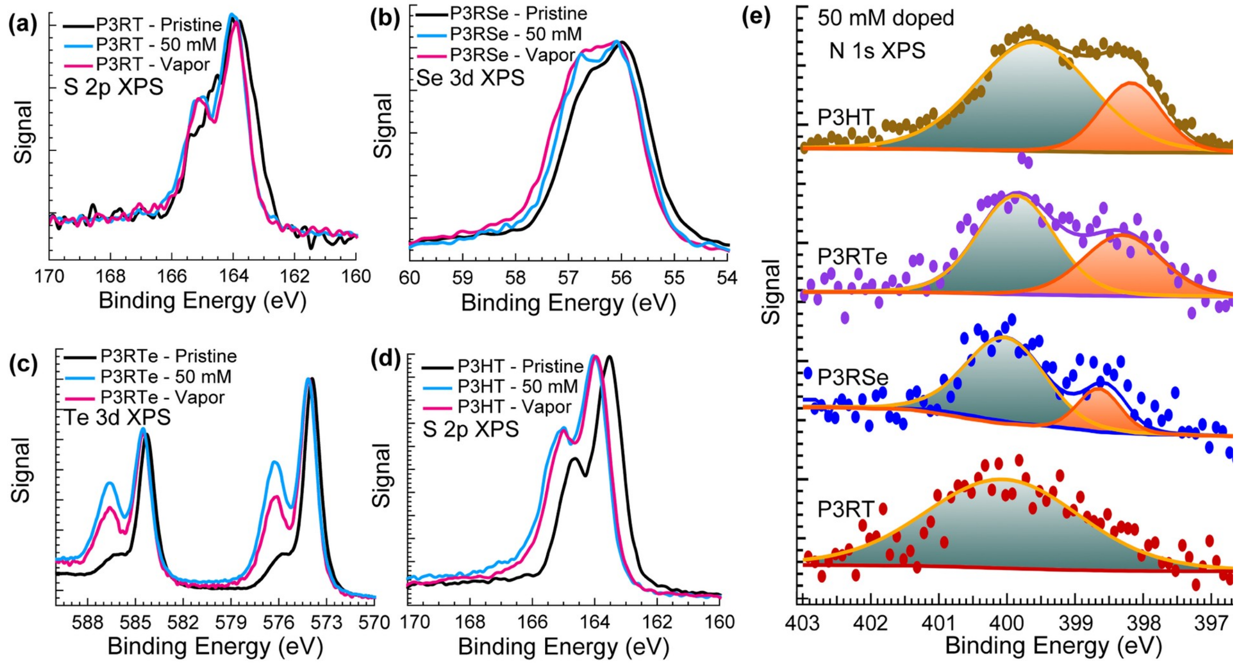

Figure 2: XPS analysis for select P3RX films. Heteroatom scans for each polymer (a) S-2p spectra in P3RT, (b) Se-3d spectra in P3RSe, (c) Te-3d spectra in P3RTe, and (d) S-2p spectra in P3HT, all demonstrate a blue shift upon doping. (e) Deconvoluted N-1s spectra of 50 mM doped polymers reveal the relative intensities of N^0 species (teal fitted peak centered at ~399.5 eV) versus the N^{-1} peak (orange fitted peak centered at ~ 398 eV). The strong presence of N^{-1} in both P3RTe and P3HT further corroborates that ICT is the dominant doping mechanism for these two polymers, as opposed to P3RT and P3RSe which show reduced or no intensity.

Deconvolution of the N-1s spectra reveals the presence of both the N^0 and N^{-1} peaks in all systems except P3RT, which demonstrates just a broad N^0 peak at ~ 399.5 eV. From the fitting of these N-1s spectra, peak area ratios were calculated to determine the relative percentage of ICT doping occurring in P3RSe, P3RTe and P3HT, which all show N^{-1} features.[32] P3RSe demonstrates a relatively low N^{-1} percentage of ~18%, further supporting the UV-VIS and FTIR measurements that ICT is not the dominant mode of charge transfer, but it is present to some extent. On the other hand, P3RTe and P3HT both demonstrate strong N^{-1} peak percentages of ~35%, suggesting that ICT is a major charge transfer mechanism at play.

Spectroscopic measurements show that the extent of doping and the mechanism vary significantly within the P3RX family, but these measurements alone do not explain why P3RT and P3RSe have significant CTC populations while P3RTe dopes primarily through ICT. Previous studies have shown that propensity for CTC or ICT doping is dependent on the method of intercalation of F4TCNQ into the polymer crystallite; specifically, CTC doping occurs as F4TCNQ resides between the crystallites' π-stacks and forms localized, hybridized polymer-F4TNCQ molecular orbitals.[13] Therefore, to probe the structural morphology of these polymers and understand the impacts of doping with F4TCNQ, grazing incidence wide angle X-ray scattering (GIWAXS) was performed on the pristine polymers and their F4TCNQ vapor-doped analogs. Vapor doped films were chosen because it has been demonstrated that this maintains higher degrees of structural ordering compared to solution doped films, and we observe comparable spectroscopic properties with both types of doping.[26,30]

A brief discussion of the pristine GIWAXS scattering shown in **Figure 3a-c** can be found in **Note S5**. Upon doping with F4TCNQ in the vapor phase, a clear change in the scattering pattern occurs for all the polymers (**Figure 3d-f**). Both P3RT and P3RSe demonstrate a contraction in lamellar lattice spacing (h00 peaks shift to higher Q), whereas P3HT and P3RTe show an expansion of the lamellar lattice (h00 peaks shift to lower Q). Focus was placed on the (100) peaks due to its strong scattering intensity. Furthermore, several studies have shown that changes in the lamellar lattice spacing can be indicative of the doping mechanism. Stanfield *et al.* demonstrated that a poor doping solvent leads to a contraction of P3HT lamellar lattice spacing, suggesting that F4TCNQ molecules coordinate within the π-π stacking region along the polymer backbone leading to CTC doping.[33] Thomas *et al.* observed a similar effect in P3HT *vs*. P3EHT, where the branched alkyl sidechains in P3EHT create steric hindrance that inhibits F4TCNQ intercalation into the polymer side chains and promotes F4TCNQ intercalation between the π-stacks, and this was accompanied by a slight decrease of the alkyl stacking distance.[13] Therefore, we postulate that P3RT and P3RSe are doped via a CTC mechanism, evidenced by the contraction in alkyl stacking distance (shift in the alkyl stacking peak to higher Q) from 22.6 nm to 19.7 nm for P3RT, and 22.4 nm to 21.5 nm for P3RSe. This suggests the dopant inserts co-facially between polymer backbones. Interestingly, while P3RTe has the same branched side chain as its thio- and seleno- counterparts, it shows a lamellar lattice expansion similar to P3HT, from 18.9 nm to 20.4 nm. This suggests that F4TCNQ intercalates in P3RTe's lamellar side chains and allows for ICT doping. There are many factors, such as crystallite size, differences in electronic interactions, etc., that could be causing these observed differences. However, we hypothesize that P3RTe's unique behavior could, in part, be due to differences in the P3RX polymers' degree of backbone rotational freedom. Ye *et al.* performed an in-depth study on the forces at work to drive crystallization in these polymers and found that as the substituted heteroatom becomes larger, there is less rotational freedom.[34] Thus, as the heteroatom becomes larger and the polymer backbone becomes more conformationally-locked in a planar configuration, the chains can come closer to one another to enable better molecular overlap which ultimately translates to higher mobility. The lower degree of backbone rotational freedom in P3RTe may hinder F4TCNQ intercalation between the π-stacks and as a result, the dopant molecules intercalate into the alkyl side chains and participate in ITC doping. In contrast, higher degrees of backbone rotational freedom in P3RSe and P3RT (while still having a sterically hindered branched alkyl side chain) translates to F4TCNQ molecules intercalating between π-stacks and participating in CTC doping, which is consistent with the spectroscopic results presented herein.

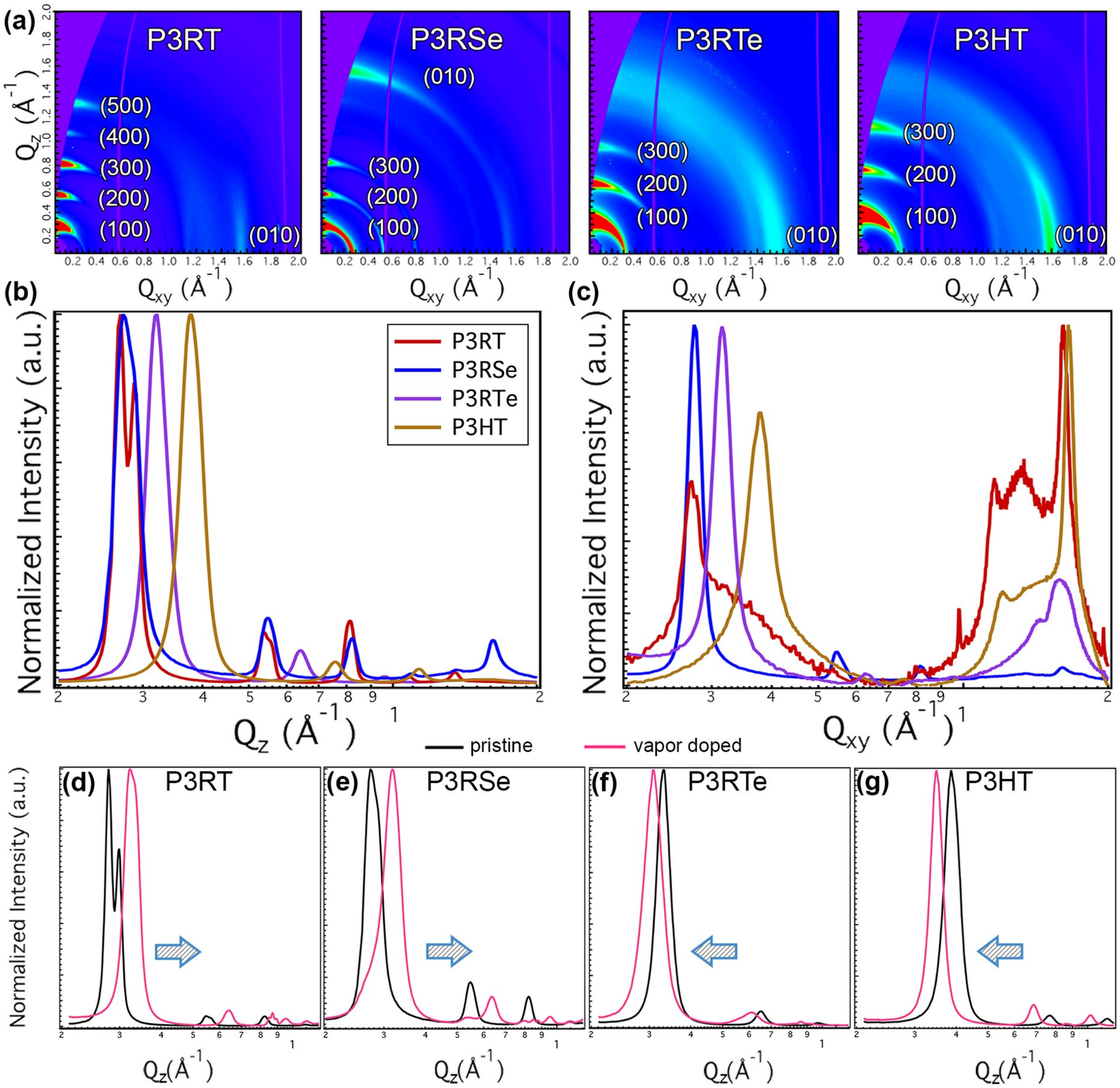

Figure 3: (a) GIWAXS of pristine polymers of P3RT, P3RSe, P3RTe and P3HT, (b) nearly out-of-plane line cuts, and (c) in-plane line cuts. The strong (h00) peaks visible in (b) along with the pronounced (010) peaks in (c) reveals preferential edge-on orientation for all the polymers except P3RSe which shows both edge-on and face-on alignment. Out-of-plane line cuts are shown for (d) P3RT, (e) P3RSe, (f) P3RTe, and (g) P3HT both before and after vapor doping with F4TCNQ. Both P3RT and P3RSe show (h00) peaks shift to higher Q after doping, indicative of a contraction of the lamellar spacing. P3RTe and P3HT show the lamellar stacking peak shift to lower Q, indicating an expansion in lamellar spacing and suggestive of F4TCNQ dopant intercalating into the alkyl side chains leading to ITC doping.

The electrical conductivity and Seebeck coefficient are a measure of the macroscopic average charge carrier density, charge carrier mobility and how these properties vary as a function of polymer chemistry and extent of doping. The P3RX family has appreciable thermoelectric properties when doped with $FeCl_3$,[10] and spectroscopic data suggests that F4TCNQ dopes all P3RX polymers and P3HT, albeit through various mechanisms. Here, these thermoelectric measurements are used to quantitatively understand to what extent ICT *vs.* CTC doping mechanisms affect the resulting charge transport.

Figure 4a plots the electrical conductivity (σ) for both the solution and vapor doped films. Although P3RT has an appreciable number of F4TCNQ dopant counterions (**Figure 2**), the number of charge carriers with sufficient mobilities is limited due to its CTC doping mechanism,[13,19] leading to a very low electrical conductivity ($\sigma < 10^{-4}$ S/cm). Similarly, P3RSe shows low electrical conductivities of $< 5\times10^{-3}$ S/cm, likely due to the dopant being incorporated between the π-stacks (**Figure 3**) resulting in a significant CTC population (**Figure 2**) with heavily localized charge carriers. The latter is supported by temperature dependent conductivity measurements, which show a large activation energy (150-200 meV), in comparison to other highly doped semiconducting polymers (<100 meV), (**Note S6**). In contrast to P3RT and P3RSe, P3RTe shows appreciable electrical conductivity at all doping concentrations in this study, with a maximum of 2.6 ± 1.1 S/cm at 25 mM F4TCNQ and with vapor doping. This is three orders of magnitude higher than P3RSe at the same doping molarity and XPS counterion concentration (**Figure 2**), owing to P3RTe being doped primarily via ITC. At a higher solution molarities of 50 mM, the electrical conductivity of P3RTe decreases, likely due to over doping, which has been reported in several polymer dopant systems.[10,12,35,36] The maximum P3RTe electrical conductivity is roughly equal to the maximum P3HT electrical conductivity of 3.2 ± 0.4 S/cm. Lastly, we note that the solution doped and vapor doped maximum electrical conductivities for P3HT and P3RTe are comparable to one another and are similar to the electrical conductivity of P3HT doped with F4TCNQ reported in previous literature.[25,30]

Now we turn to analyze the Seebeck coefficient in **Figure 4b**. The Seebeck coefficient (S) is directly related to the asymmetry of the carrier distribution about the Fermi energy. Thus, S usually decreases as a result of reduced asymmetry as carrier concentration increases. Doped P3RT and P3RSe films were too insulating for repeatable Seebeck coefficients to be reported, while both P3RTe and P3HT show observable Seebeck coefficients. As expected, the Seebeck coefficient decreases as the doping concentration increases for both P3RTe and P3HT; further discussion can be found in **Note S6**. This trend agrees with the measured increasing electrical conductivity and increasing charge carrier concentration, as well as previous literature reports.

Lastly, we examine the S-σ plot for the P3RX polymers doped with $FeCl_3$ and F4TCNQ (**Figure 4c**). The curvature, slope, and nominal values on the S-σ plot are indicative of fundamental transport phenomena, so analyzing these curves enables rational polymer and dopant design for optimal thermoelectric performance.[37] Although the values in **Figure 4c** do not lead to record-high thermoelectric power factors (maximum of *ca.* 3.8 $\mu W/mK^2$ for the P3RTe-F4TCNQ films), it is notable that all P3RX-$FeCl_3$ and P3RTe-F4TCNQ datasets lie on the same curve. According to the Kang-Snyder model, a generalized transport model developed for polymers, materials that lie on the same curve have a similar set of governing transport physics (*e.g.* mobilities, energy dependence, electronic structures).[37] Based on this framework, we find that the heteroatom, dopant concentration, and chemistry are all parameters that shift transport properties along the same S-σ curve, but do not laterally or vertically shift the S-σ curve (as long as the polymers are doped via ICT mechanisms). Therefore, we hypothesize that in addition to using poly(tellurophenes) for their advantageous ordering and doping susceptibility, employing additional orienting methods such as drawing,[38] or rubbing,[18,39] which have been shown to laterally shift the S-σ curve, will likely lead to enhanced thermoelectric performance beyond what is reported in this work.

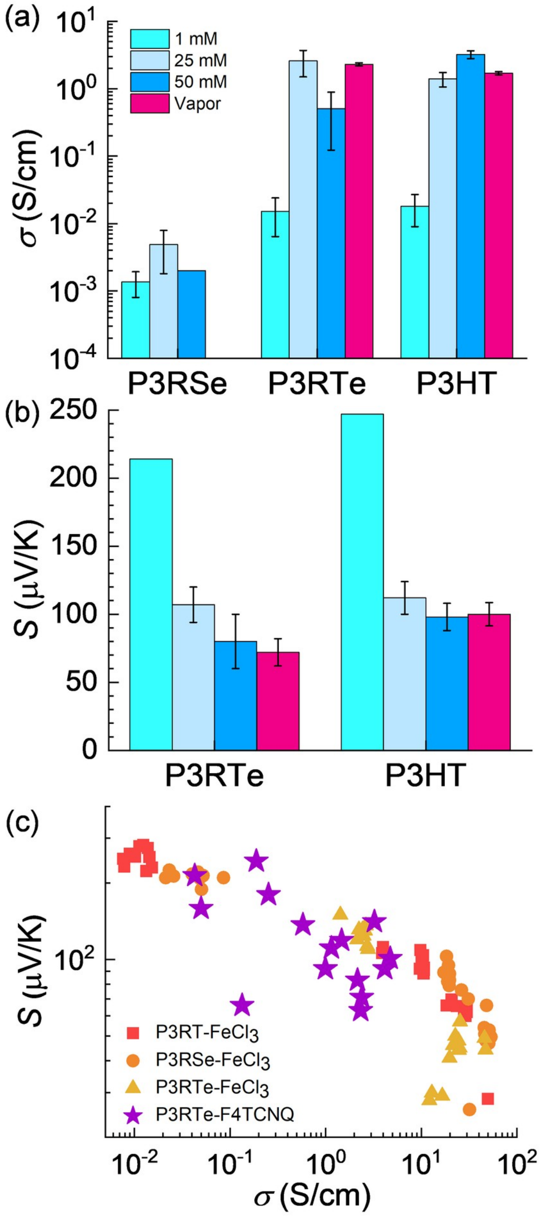

Figure 4: Thermoelectric properties as a function of heteroatom and doping. (a) Electrical conductivity, (b) Seebeck coefficient, (c) Jonker curve comparing this study (P3RTe-F4TCNQ) with our previously reported P3RX-FeCl$_3$ dataset. Error bars, when present, represent the sample-to-sample standard deviation.

In this work, we demonstrated that varying the heteroatom (S, Se, Te) alters the polymer microstructure, doping mechanism, and charge transport properties. Moving from S to Se to Te, the susceptibility to F4TCNQ doping increases. Optical and photoelectron spectroscopies suggest that all P3RX polymers have a comparable number of F4TCNQ counterions, but P3RT is not heavily oxidized and is doped dominantly via CTC mechanisms, P3RSe is more oxidized and is likely doped through both CTC and ICT, and that P3RTe is heavily oxidized and primarily doped through ICT. GIWAXS measurements suggest that P3RT and P3RSe are prone to CTC doping because of their microstructural ordering, resulting in dopant intercalation between π-stacks. In contrast, P3RTe is similar to P3HT (ICT) because of its planar packing that enables dopant intercalation into the lamellar side chains. Lastly, we note that P3RTe/F4TCNQ has similar transport properties to P3RX/$FeCl_3$, suggesting that more sophisticated processing techniques (*e.g.* rubbing, drawing) may be needed to laterally shift the S-σ curve for the P3RX family. The observations herein quantify how polymer and dopant synthetic engineering (heteroatom, side chain, microstructure, dopant chemistry) affect charge transport and provides guidance for future improvement of semiconducting polymers.

Supporting Information Contents:

Funding: MPG and JPW gratefully acknowledge support from the National Science Foundation Graduate Research Fellowship. SAG appreciates the partial support from the Office of Naval Research (award number N00014-19-1-2162), the Department of Education Graduate Assistance in Areas of National Need (GAANN) program at the Georgia Institute of Technology (Award #P200A180075), the Link Energy Foundation, and the Science and Technology of Material Interfaces (STAMI) group at the Georgia Institute of Technology. SY and DSS are grateful for support from the NSERC of Canada and the University of Toronto Connaught Foundation for a McLean Award.

This work was performed in part at the Molecular Foundry and the Advanced Light Source (beamline 7.3.3), Lawrence Berkeley National Laboratory, and was supported by the Department of Energy, Office of Science, Office of Basic Energy Sciences, Scientific User Facilities Division of the U.S. Department of Energy under Contract No. DE-AC02-05CH11231. Part of this work was also performed at the Georgia Tech Institute for Electronics and Nanotechnology, a member of the National Nanotechnology Coordinated Infrastructure, which is supported by the National Science Foundation (Grant ECCS-1542174).

Data Availability Statement: The data that supports the findings of this study are available within the article and its supplementary material.

ReferencesX1 R. Kroon, D. A. Mengistie, D. Kiefer, J. Hynynen, J. D. Ryan, L. Yu, and C. Muller, Chem Soc Rev **45** (22), 6147 (2016).

2 Olga Bubnova and Xavier Crispin, Energy & Environmental Science **5** (11) (2012).

3 James F. Ponder Jr, Akanksha K. Menon, Raghunath R. Dasari, Sandra L. Pittelli, Karl J. Thorley, Shannon K. Yee, Seth R. Marder, and John R. Reynolds, Advanced Energy Materials **9** (24), 1900395 (2019).

4 Hend M. Elmoughni, Akanksha K. Menon, Rylan M. W. Wolfe, and Shannon K. Yee, Advanced Materials Technologies **4** (7), 1800708 (2019).

5 Akanksha K. Menon, Olivia Meek, Arnold J. Eng, and Shannon K. Yee, Journal of Applied Polymer Science **134** (3) (2017).

6 Jon Hollinger, Dong Gao, and Dwight S. Seferos, Israel Journal of Chemistry **54** (5-6), 440 (2014).

7 Elisa I. Carrera and Dwight S. Seferos, Macromolecules **48** (2), 297 (2014).

8 A. A. Jahnke, B. Djukic, T. M. McCormick, E. Buchaca Domingo, C. Hellmann, Y. Lee, and D. S. Seferos, J Am Chem Soc **135** (3), 951 (2013).

9 Lianshan Li, Jon Hollinger, Ashlee A. Jahnke, Srebri Petrov, and Dwight S. Seferos, Chemical Science **2** (12) (2011).

10 Shawn A. Gregory, Akanksha K. Menon, Shuyang Ye, Dwight S. Seferos, John R. Reynolds, and Shannon K. Yee, Advanced Energy Materials **8** (34) (2018).

11 Joseph G. Manion, Shuyang Ye, Andrew H. Proppe, Arnaud W. Laramée, George R. McKeown, Emily L. Kynaston, Shana O. Kelley, Edward H. Sargent, and Dwight S. Seferos, ACS Applied Energy Materials **1** (9), 5033 (2018).

12 Hio-Ieng Un, Shawn A. Gregory, Swagat K. Mohapatra, Miao Xiong, Elena Longhi, Yang Lu, Sergei Rigin, Samik Jhulki, Chi-Yuan Yang, Tatiana V. Timofeeva, Jie-Yu Wang, Shannon K. Yee, Stephen Barlow, Seth R. Marder, and Jian Pei, Advanced Energy Materials **9** (24) (2019).

13 Elayne M. Thomas, Emily C. Davidson, Reika Katsumata, Rachel A. Segalman, and Michael L. Chabinyc, ACS Macro Letters **7** (12), 1492 (2018).

14 P. Y. Yee, D. T. Scholes, B. J. Schwartz, and S. H. Tolbert, J Phys Chem Lett, 4929 (2019).

15 Zhiming Liang, Yadong Zhang, Maryam Souri, Xuyi Luo, Alex M Boehm, Ruipeng Li, Yan Zhang, Tairan Wang, Doo-Young Kim, Jianguo Mei, Seth R. Marder, and Kenneth R. Graham, Journal of Materials Chemistry A **6** (34), 16495 (2018).

16 Sandra L. Pittelli, Shawn A. Gregory, James F. Ponder, Shannon K. Yee, and John R. Reynolds, Journal of Materials Chemistry C **8** (22), 7463 (2020).

17 Jeffrey J. Urban, Akanksha K. Menon, Zhiting Tian, Anubhav Jain, and Kedar Hippalgaonkar, Journal of Applied Physics **125** (18), 180902 (2019).

18 Viktoriia Untilova, Till Biskup, Laure Biniek, Vishnu Vijayakumar, and Martin Brinkmann, Macromolecules (2020).

19 Kristen E. Watts, Bharati Neelamraju, Erin L. Ratcliff, and Jeanne E. Pemberton, Chemistry of Materials **31** (17), 6986 (2019).

20 O. Zapata-Arteaga, B. Dorling, A. Perevedentsev, J. Martin, J. S. Reparaz, and M. Campoy-Quiles, Macromolecules **53** (2), 609 (2020).

21 H. Mendez, G. Heimel, S. Winkler, J. Frisch, A. Opitz, K. Sauer, B. Wegner, M. Oehzelt, C. Rothel, S. Duhm, D. Tobbens, N. Koch, and I. Salzmann, Nat Commun **6**, 8560 (2015).

22 D. Kiefer, R. Kroon, A. I. Hofmann, H. Sun, X. Liu, A. Giovannitti, D. Stegerer, A. Cano, J. Hynynen, L. Yu, Y. Zhang, D. Nai, T. F. Harrelson, M. Sommer, A. J. Moule, M. Kemerink, S. R. Marder, I. McCulloch, M. Fahlman, S. Fabiano, and C. Muller, Nat Mater **18** (2), 149 (2019).

23 D. Tyler Scholes, Patrick Y. Yee, Jeffrey R. Lindemuth, Hyeyeon Kang, Jonathan Onorato, Raja Ghosh, Christine K. Luscombe, Frank C. Spano, Sarah H. Tolbert, and Benjamin J. Schwartz, Advanced Functional Materials **27** (44) (2017).

24 J. Hynynen, D. Kiefer, L. Yu, R. Kroon, R. Munir, A. Amassian, M. Kemerink, and C. Muller, Macromolecules **50** (20), 8140 (2017).

25 Ian E. Jacobs, Erik W. Aasen, Julia L. Oliveira, Tayane N. Fonseca, John D. Roehling, Jun Li, Gwangwu Zhang, Matthew P. Augustine, Mark Mascal, and Adam J. Moulé, J. Mater. Chem. C **4** (16), 3454 (2016).

26 Eunhee Lim, Kelly A. Peterson, Gregory M. Su, and Michael L. Chabinyc, Chemistry of Materials **30** (3), 998 (2018).

27 B. Neelamraju, K. E. Watts, J. E. Pemberton, and E. L. Ratcliff, J Phys Chem Lett **9** (23), 6871 (2018).

28 Jonathan K. Harris, Bharati Neelamraju, and Erin L. Ratcliff, Chemistry of Materials **31** (17), 6870 (2019).

29 K. E. Watts, B. Neelamraju, M. Moser, I. McCulloch, E. L. Ratcliff, and J. E. Pemberton, J Phys Chem Lett **11** (16), 6586 (2020).

30 Matthew T. Fontana, Dane A. Stanfield, D. Tyler Scholes, K. J. Winchell, Sarah H. Tolbert, and Benjamin J. Schwartz, The Journal of Physical Chemistry C **123** (37), 22711 (2019).

31 Ban Xuan Dong, Christian Nowak, Jonathan W. Onorato, Tengzhou Ma, Jens Niklas, Oleg G. Poluektov, Garrett Grocke, Mark F. DiTusa, Fernando A. Escobedo, Christine K. Luscombe, Paul F. Nealey, and Shrayesh N. Patel, Chemistry of Materials **33** (2), 741 (2021).

32 Haiyuan Wang, Sergey V. Levchenko, Thorsten Schultz, Norbert Koch, Matthias Scheffler, and Mariana Rossi, Advanced Electronic Materials **5** (5), 1800891 (2019).

33 Dane A. Stanfield, Yutong Wu, Sarah H. Tolbert, and Benjamin J. Schwartz, Chemistry of Materials (2021).

34 S. Ye, L. Janasz, W. Zajaczkowski, J. G. Manion, A. Mondal, T. Marszalek, D. Andrienko, K. Mullen, W. Pisula, and D. S. Seferos, Macromol Rapid Commun **40** (1), e1800596 (2019).

35 Khaled Al Kurdi, Shawn A. Gregory, Samik Jhulki, Maxwell Conte, Stephen Barlow, Shannon K. Yee, and Seth R. Marder, Materials Advances **1** (6), 1829 (2020).

36 Shawn A. Gregory, Yi Li, Timothy D. Monroe, Junjian Li, Shannon K. Yee, and Mark D. Losego, ACS Applied Polymer Materials **3** (2), 720 (2021).

37 S. Dongmin Kang and G. Jeffrey Snyder, Nat Mater **16** (2), 252 (2017).

38 J. Hynynen, E. Jarsvall, R. Kroon, Y. Zhang, S. Barlow, S. R. Marder, M. Kemerink, A. Lund, and C. Muller, ACS Macro Lett **8** (1), 70 (2019).

39 Vishnu Vijayakumar, Yuhan Zhong, Viktoriia Untilova, Mounib Bahri, Laurent Herrmann, Laure Biniek, Nicolas Leclerc, and Martin Brinkmann, Advanced Energy Materials **9** (24) (2019).